Energy 348 (2026) 140537

Contents lists available at ScienceDirect

Energy

journal homepage: www.elsevier.com/locate/energy

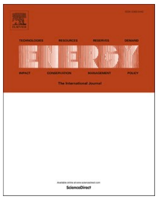

Influence of turbine damping on OWC wave-to-wire performance

I. López [a], B. Álvarez [a], D.M. Fouz [b], R. Carballo [a,*], G. Iglesias [c,d]

[a] *Área de Ingeniería Hidráulica, EPSE, Campus Terra, Universidade de Santiago de Compostela, 27002, Lugo, Spain*
[b] *PROePLA (GI-1716), Área de Proyectos de Ingeniería, EPSE, Campus Terra, Universidade de Santiago de Compostela, 27002, Lugo, Spain*
[c] *School of Engineering and Architecture & MaREI, Environmental Research Institute, University College Cork, College Road, P43 C573, Cork, Ireland*
[d] *School of Engineering, Computing and Mathematics, University of Plymouth, Marine Building, Drake Circus, PL4 8AA, Plymouth, UK*

ARTICLE INFO

Keywords:
Oscillating water column
Turbine-induced damping
Turbine-chamber coupling
Physical modelling
Wave-to-wire modelling
Impulse turbine

ABSTRACT

Turbine-chamber coupling is a decisive factor in the performance of oscillating water column (OWC) wave energy converters. In this study, a wave-to-wire model is developed to evaluate the influence of turbine-induced damping on the different energy conversion stages—pneumatic, mechanical, and electrical—of an OWC equipped with a biradial turbine. The methodology combines: (i) high-resolution spectral modelling to characterize the nearshore wave energy resources at a study site in Galicia (NW Spain); (ii) physical (laboratory) and computational fluid dynamics (CFD) modelling of the OWC hydrodynamics accounting for air compressibility; and (iii) analytical modelling of the turbine–generator set, including a control law for rotational speed regulation. Results show that turbine-induced damping critically affects the performance of OWC devices across all energy conversion stages, with the optimal damping condition varying according to the stage considered. Mechanical efficiency emerges as a key factor, which can shift the optimal damping towards higher values than those indicated by the pneumatic efficiency alone. These findings underscore the importance of turbine efficiency in OWC design and highlight the need to integrate mechanical and electrical conversion stages into turbine-chamber coupling strategies to achieve optimal performance.

1. Introduction

In the context of growing energy demand and the need to reduce greenhouse gas emissions, the development of renewable energy sources has become increasingly critical [1]. Among renewables, wave energy stands out due to its huge potential, with a theoretical global annual production estimated at 29500 TWh [2]. In addition, wave energy offers advantages such as high predictability [3], relative low environmental impact [4,5] and high energy density, not least at certain coastal locations [6]. As a result, significant efforts have been devoted over the last decades to the development of wave energy converters (WECs) capable of harvesting this resource efficiently and reliably [7,8].

Among the wide range of WEC concepts proposed, oscillating water column (OWC) devices have attracted considerable attention due to their simplicity, ease of maintenance and versatility [9]. Building on this versatility, a variety of OWC configurations have been investigated, including breakwater-integrated devices [10], devices attached to energy-focusing breakwaters [11,12], floating offshore systems [13], multi-OWC platforms [14], OWCs integrated into tubular structures [15,16], and hybrid solutions, either combined with other WECs [17] or integrated into offshore wind turbine foundations [18,19]. An OWC consists of a hollow, semi-submerged chamber that is open to the sea below the free water surface and connected with the atmosphere above the free surface through an air turbine. Incident waves cause the water column inside the chamber to oscillate, so that it compresses and decompresses the air above. This process generates an oscillatory air flow between the interior of the chamber and the atmosphere that drives the turbine-generator set. Several solutions have been proposed to harness the bidirectional flow, including twin unidirectional turbines [20,21] and vented OWC devices, which use passive air flow valves in the chamber to rectify the flow [22,23]. However, the most widely adopted solution is self-rectifying air turbines [24].

Initially, the Wells reaction turbine [25] was the most common self-rectifying turbine used in OWC converters, which exhibits a high peak efficiency; however, its efficient flow range is narrow, with performance dropping sharply outside this range due to rotor blade stalling. For this reason, attention has shifted in recent years to self-rectifying impulse turbines, which provide a broader operational range [26]. Among them, the recently developed biradial turbine [27,28] is particularly promising. Its design, symmetric with respect to a plane perpendicular to its axis of rotation, combines centripetal inflow and

---

* Corresponding author.
E-mail address: rodrigo.carballo@usc.es (R. Carballo).

https://doi.org/10.1016/j.energy.2026.140537
Received 9 October 2025; Received in revised form 19 February 2026; Accepted 21 February 2026

Nomenclature

Roman symbols

a	generator control law constant
A_c	plan area of the OWC chamber (m^2)
b	generator control law exponent
B_c	dimensionless damping coefficient of the chamber (–)
B_t	dimensionless damping coefficient of the turbine (–)
C_g	group velocity of waves (m/s)
d	orifice diameter in OWC chamber model (m)
D	turbine rotor diameter (m)
g	acceleration of gravity (m/s^2)
H	wave height (m)
H_m0	spectral significant wave height (m)
I	turbine-generator set moment of inertia (kg m^2)
K	damping constant (kg/m^7)
$\dot{m}_\mathrm{t}$	turbine mass flow rate (kg/s)
P_e	electrical power (W)
P_g	generator electromagnetic power (W)
P_p	pneumatic power (W)
P_t	turbine aerodynamic power (W)
P_w	wave power per metre of wave front (W/m)
Q	air flow rate (m^3/s)
S	wave energy spectral density (m^2/Hz)
t	time (s)
T	wave period (s)
T_g	generator control torque (N m)
T_e	wave energy period (s)
w_c	width of the OWC chamber (in direction parallel to wave fronts) (m)
z	elevation of the water column free surface (m)

Greek

Δp	pressure drop (Pa)
η_e	electrical efficiency (–)
η_m	mechanical efficiency (–)
η_p	pneumatic efficiency (–)
η_t	turbine efficiency (–)
ξ_a	aerodynamic capture-width ratio (–)
ξ_e	electrical capture-width ratio (–)
ξ_h	hydrodynamic capture-width ratio (–)
Π	turbine dimensionless power (–)
ρ	fluid density (kg/m^3)
Φ	turbine dimensionless flow rate (–)
Ψ	turbine dimensionless pressure head (–)
Ω	turbine/generator set rotational speed (rad/s)

centrifugal outflow, and offers the high efficiency characteristic of the Wells turbine and the wide operating range of impulse turbines.

Turbine and chamber play central roles in determining the overall performance of an OWC device. However, the performance of the system depends not only on the characteristics of these elements individually, but also on the coupling between them or, more specifically, the turbine-induced damping [29,30]. Previous studies investigated the effects of turbine-induced damping on OWC efficiency using Particle Image Velocimetry [31] or Artificial Neural Networks [32]. Methodologies have been developed to optimize turbine-induced damping for specific wave conditions [33] and for site-specific wave climates [34]. More recently, a procedure has been proposed to link the turbine diameter to the turbine-induced damping that maximizes pneumatic power capture [35]. Typically, the capture-width ratio—defined as the ratio of the pneumatic power captured by the chamber to the incident wave power—has been the primary metric for assessing the performance of the device [e.g., [36,37]]. However, an OWC involves two additional energy conversion stages: from pneumatic to mechanical power, and from mechanical to electrical power. A performance metric that considers only the conversion from wave power to pneumatical power does not suffice. It is essential to assess the influence of the turbine-induced damping on the final electrical output of the device and to determine whether the damping that maximizes the capture-width ratio also maximizes electrical power.

To predict the overall performance of an OWC device, as well as the efficiencies achieved at each energy conversion stage, wave-to-wire (W2W) models that explicitly represent the hydrodynamic, aerodynamic, and electrical subsystems are essential [38]. Traditionally, analytical W2W models have been the most widely adopted approach. For instance, Ciappi et al. [39,40] applied an analytical W2W model, based on the rigid-piston approximation, to optimize an OWC converter operating under moderate wave conditions in the Mediterranean Sea, comparing the performance of Wells and impulse turbines. Rosati and Ringwood [41] further examined W2W efficiency maximization by modulating the rotational speed of a Wells turbine, demonstrating that an appropriate speed control can enhance overall energy conversion through improvements in the hydrodynamic performance. Computational fluid dynamic (CFD) approaches have also been employed for W2W modelling. Liu et al. [42,43] presented an integrated chamber-turbine model based on the Reynolds-averaged Navier-Stokes (RANS) equations, capable of simulating the complete operating process of an OWC system under different wave conditions and predicting primary-stage, secondary-stage, and overall efficiencies. More recently, Ding et al. [44] presented a W2W time-domain model encompassing the full energy conversion chain—from chamber dynamics to turbine behaviour and a permanent magnet synchronous generator (PMSG)—to evaluate the output power and stage-by-stage conversion efficiency. This model was subsequently extended [45] by incorporating an adjustable resistive load, enabling the analysis of its influence on system behaviour and demonstrating its potential to enhance the OWC overall performance.

Within this framework, the objective of the present study is to develop a W2W model capable of assessing the influence of the turbine-induced damping across the various energy conversion stages of an OWC wave energy converter equipped with an impulse turbine, specifically, a biradial turbine. In contrast to previous studies that focus primarily on pneumatic performance, the approach presented here enables a comprehensive analysis of the entire energy conversion chain, from the wave resources to the electrical output. To this end, a hybrid modelling approach is employed, integrating: (i) high-resolution spectral numerical modelling to characterize the wave energy resource at the study site, (ii) physical and CDF modelling to evaluate the hydrodynamics of the device, and (iii) analytical modelling to represent the turbine-generator set dynamics. The approach is illustrated through a case study at a coastal location in Galicia (NW Spain).

The structure of the paper is as follows. Materials and methods are described in Section 2, including the characterization of the wave energy resource at the study site, the wave-WEC interaction modelling, the turbine-generator set modelling and the performance evaluation procedure. Results are presented and discussed in Section 3. Finally, conclusions are drawn in Section 4.

2. Materials and methods

2.1. Wave energy resources

In assessing wave energy resources, it is important to bear in mind the variability of sea states and their frequency of occurrence. For these reasons, considering the performance of an OWC device under one or a few individual sea states may result in an incomplete picture. A more complete picture may be formed by considering the total energy output in a typical year at the site of interest. For that purpose, the wave climate must be characterized in terms of the distribution of sea states—their wave heights and periods, and their frequencies of occurrence in a typical year.

With this in view, a coastal site in Galicia (NW Spain) is selected as a case study, with coordinates $X = 510281.79$ m, $Y = 4677697.00$ m (WGS84-UTM29N). This site was identified in previous research as suitable for wave energy exploitation [46]. The corresponding wave energy characterization matrix is presented in Fig. 1. It was obtained using the WEDGE methodology [3,47], which accounts for virtually the entire deepwater wave energy resources and their propagation towards the coast using high-resolution spectral numerical modelling. The *energy bins*—bivariate intervals of significant wave height and energy period [48]—that contribute the most to the total annual wave energy correspond to sea states with energy periods (T_e) between 8 and 11 s and spectral significant wave heights (H_{m0}) between 1 and 3 m.

2.2. Wave-WEC interaction modelling

The hydrodynamics of the OWC device was characterized by means of a combination of physical (laboratory) and numerical modelling. First, laboratory tests were carried out to establish the interaction between incident waves and the OWC chamber. Their main output was the time-varying pressure drop between the interior of the chamber and the atmosphere. Second, numerical modelling was applied to establish the relationship between pressure drop and flow rate, enabling the calculation of the flow rate from the experimentally obtained pressure data. This step is essential because, when considering air compressibility, the air flow rate cannot be directly calculated from the motions of the free surface inside the chamber, and direct measurements are not feasible [49].

The physical model reproduces an L-shaped device (Fig. 2) at a 1:30 scale. The defining characteristic of an L-shaped OWC is the geometry of the chamber, which presents an elongated submerged section oriented in the direction of wave incidence [50]. This design is conducive to near-resonant conditions for relatively long wave periods, even in shallow waters. The dimensions of the model are based on previous work [51], in which an optimization procedure was performed to tune the natural period of oscillation of the chamber to wave periods around 10 s.

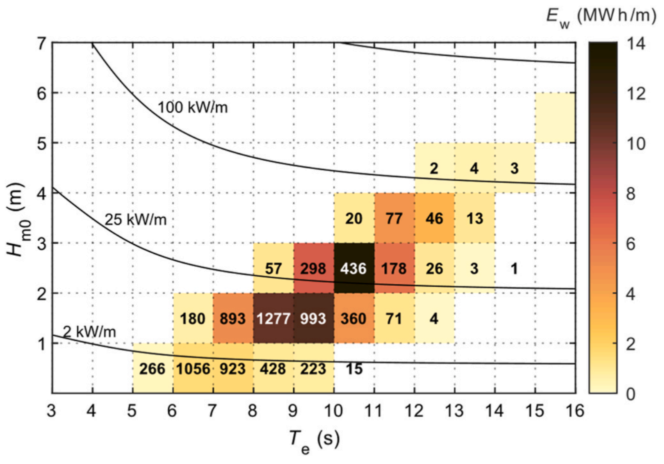

Fig. 1. Wave energy resource characterization matrix at the study site. The colour scale indicates the contribution to the total annual wave energy per metre of wave front (E_w) of the sea states in each energy bin. The numerical value in each energy bin is its occurrence expressed in hours in an average year. The overlaid curves represent wave power isolines.

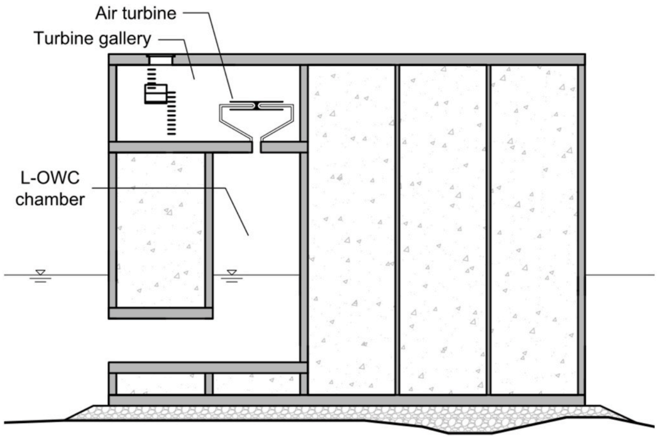

Fig. 2. Conceptual scheme of an L-shaped OWC integrated into a caisson breakwater.

The OWC model was designed according to the Froude similitude, ensuring equality of the inertia-to-gravity force ratio between model and prototype, and perfect geometric similarity in the wet part of the model, as required for free-surface flows [52]. This assumption, however, implies distorting the ratios between other force pairs. For example, the ratios of inertia to viscous forces (Reynolds number) and inertia to surface tension forces (Weber number) differ between model and prototype, which may influence, among other effects, the thermodynamic behaviour of the system, although the relevance of this effect is yet to be analysed in depth [53]. Similarly, Froude scaling does not preserve the ratio between inertia and air compression forces. Nevertheless, air compressibility is known to significantly influence the performance of full-sized OWC devices and constitutes an important scale effect if not properly represented [49,54]. In this work, to account for air compressibility, the air volume of the chamber was increased by means of an auxiliary air reservoir of appropriate dimensions, following the procedure described in Ref. [55].

Regarding the turbine, it is generally not feasible to represent it by means of a small-scale turbine that simultaneously preserves all the factors affecting its performance—such as rotor inertia and friction effects—primarily due to the small scale ratios involved. As a result, turbines are common replaced by passive elements, such as orifices or porous materials, that provide a simplified representation of the turbine-induced damping [9]. In the present study, orifices were used to approximate the quadratic relationship between pressure and flow rate associated with self-rectifying impulse turbines. Despite its simplifications, such as the inability to capture turbine-specific transient behaviour associated with rotor dynamics, the use of orifices is a widely used approach in small-scale OWC tests (e.g., Refs. [34,50]) and allows the hydrodynamic response of the system to be investigated over a range of damping conditions. A comprehensive discussion of scale effects and associated limitations in OWC physical modelling is provided in Ref. [53].

The experimental campaign was conducted in the wave flume at the University of Santiago de Compostela (USC) to evaluate the hydrodynamic performance of the OWC device under an extensive range of irregular wave conditions. These conditions were selected to represent nearly all the potential sea states that could contribute to energy production at virtually any location of interest. Specifically, tests were performed to cover energy bins with energy periods ranging from 4 to 15 s at 1-s intervals, and spectral significant wave heights up to 5 m, at 1-m intervals. This resulted in a total of 42 wave conditions tested, each corresponding to a specific energy bin (Fig. 3). With this approach, the experimental campaign encompasses virtually the entire exploitable wave energy resource at the selected site (Section 2.1). Each wave condition was tested under eight levels of turbine-induced damping,

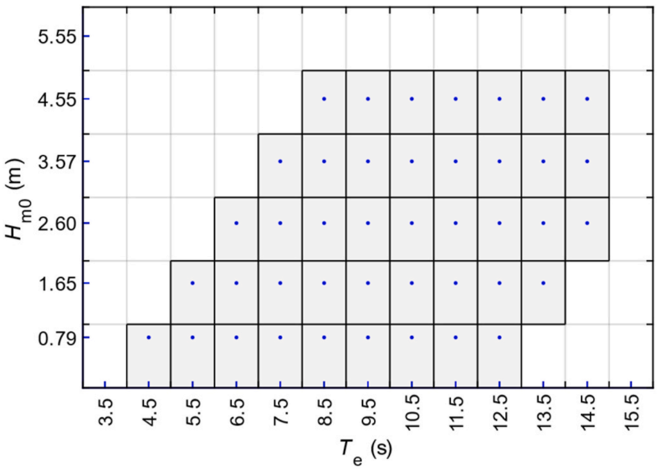

Fig. 3. Matrix of the experimentally tested wave conditions (in prototype dimensions). The point in each bin indicates the representative wave condition of that bin.

simulated by means of orifices with different diameters: $d = 9$, 12, 14, 17, 20, 22, 25 and 29 mm. A detailed description of the tests and the experimental set-up is provided in Ref. [35].

To determine the flow rate through each orifice—which is required in conjunction with pressure measurements to calculate the pneumatic power captured by the OWC—a numerical model, reproducing the physical wave flume at USC, was developed. The model is based on the Navier-Stokes equations for two compressible fluids. It was implemented using the *compressibleInterFoam* multiphase solver from the OpenFOAM software [56], which enables air compressibility to be properly simulated. The volume-of-fluid method was used for interface capturing. For wave generation, the *waves2Foam* toolbox [57], based on the relaxation zone technique, was employed. Regarding turbulence, the k-ω-SST model was selected [58]. A comprehensive description of the numerical model, including the governing equations, computational domain, and boundary conditions is provided in Ref. [35].

To validate the numerical model, the differential air pressure between the atmosphere and the interior of the chamber, as well as the water column oscillations at two locations—one near the front wall and other near the rear wall—were measured in experimental tests. Pressure measurements were obtained using a Druck-Unik5000 differential pressure sensor (measurement range ±3400 Pa and accuracy ±0.04% of full scale), while water column oscillations were recorded using two Honeywell 943-F4V ultrasonic level sensors (accuracy ±1 mm). The measured time series were compared with the corresponding results from the numerical simulations for orifice diameters of $d = 17$, 20, 22 and 25 mm. Since the pressure-flow rate curve of a given orifice diameter does not vary significantly with the wave conditions [49], the model was evaluated under four regular wave cases: $(H, T) = (0.033\text{ m}, 1.46\text{ s})$; $(0.050\text{ m}, 1.64\text{ s})$; $(0.067\text{ m}, 1.83\text{ s})$; and $(0.083\text{ m}, 2.01\text{ s})$, all expressed in model-scale dimensions.

Once validated, the numerical model was used to calculate the constant relating pressure drop and flow rate for each orifice:

$$K = \frac{\Delta p}{Q^2}, \tag{1}$$

where Q is the flow rate through the orifice. The value of K for each orifice was obtained by adjusting a parabola to the data points of the different tests, following the procedure detailed in Ref. [29]. Applying dimensional analysis, K can be non-dimensionalized as follows:

$$B_c = \frac{\Delta p^{1/2}}{Q}\frac{A_c}{\rho_w^{1/2}} = K^{1/2}\frac{A_c}{\rho_w^{1/2}}, \tag{2}$$

where A_c is the plan area of the chamber and ρ_w is the water density. Incidentally, the use of water density to non-dimensionalize the damping coefficient is essential given that experimental tests are performed with fresh water and OWCs in the sea operate with denser water. The parameter thus obtained, B_c, is denominated *dimensionless damping coefficient* of the chamber and will be useful below in dimensioning the turbine.

The flow rate time series were obtained from the measured pressure drop time series and the corresponding K values of each orifice by means of the following relationship:

$$Q = \operatorname{sgn}(\Delta p)\left(\frac{|\Delta p|}{K}\right)^{1/2}. \tag{3}$$

2.3. Turbine-generator set modelling

2.3.1. Turbine dimensioning

Each orifice tested in the experimental campaign introduces a certain amount of damping in the oscillations of the water column, which is equivalent to the damping produced by a certain non-linear air turbine [59]. To determine the diameter of the turbine of equivalent damping, a procedure based on dimensional analysis was developed in Ref. [35]. For the reader's convenience, the procedure is outlined below.

The performance characteristics of an air turbine can be expressed in dimensionless form through the pressure head (Ψ), flow rate (Φ) and power (Π) coefficients:

$$\Psi = \frac{\Delta p}{\rho_{in}\,\Omega^2 D^2}, \tag{4}$$

$$\Phi = \frac{\dot{m}_t}{\rho_{in}\,\Omega D^3}, \tag{5}$$

$$\Pi = \frac{P_t}{\rho_{in}\,\Omega^3 D^5}, \tag{6}$$

where Δp is the turbine pressure head; ρ_{in} is the air density at the turbine inlet; Ω is the rotational speed of the turbine; D is the rotor diameter; $\dot{m}_t$ is the mass flow rate of air through the turbine; and P_t is the instantaneous aerodynamic power of the turbine. Its efficiency is defined as:

$$\eta_t = \frac{\Pi}{\Phi\Psi}. \tag{7}$$

The performance curves for the biradial turbine are presented in

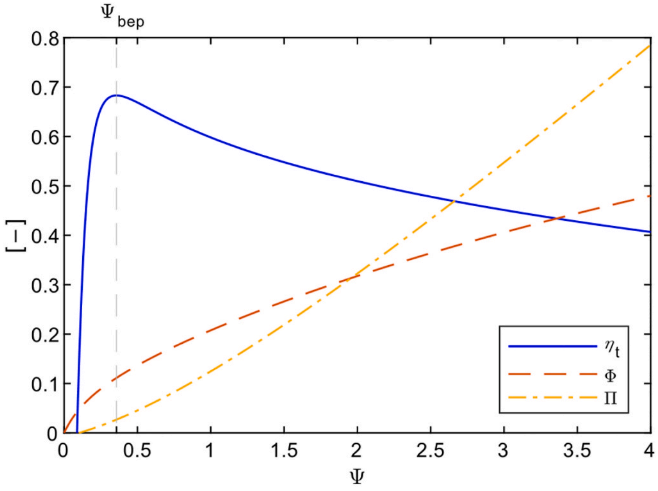

Fig. 4. Flow rate (Φ) and power (Π) coefficients and efficiency (η_t) as a function of the pressure head coefficient (Ψ) for a biradial turbine. $\Psi_{bep} = 0.357$, $\Pi_{bep} = 0.027$. Adapted from Ref. [60].

Fig. 4. Based on the previous coefficients, the dimensionless damping coefficient of the turbine can be defined as [35]:

$$B_t = \frac{Q}{\Delta p^{1/2}} \frac{\rho_a^{1/2}}{D^2}. \tag{8}$$

Oscillations in air pressure are assumed to be small relative to atmospheric pressure; therefore, variations in air density are neglected ($\rho_{in} = \rho_a$).

Finally, combining Eqs. (2) and (8), the diameter of the biradial turbine with equivalent damping to a certain orifice diameter can be determined using [35]:

$$D = \left(\frac{A_c\, \rho_a^{1/2}}{B_t\, B_c\, \rho_w^{1/2}}\right)^{1/2}. \tag{9}$$

Based on previous works, the value of B_t is set to 0.186, which corresponds to the dimensionless pressure head under which the best efficiency is achieved [35]. Therefore, once the optimal damping of the chamber is identified ($B_{c,bep}$), the turbine dimensioned following Eq. (9) will provide this level of damping while overall operating at maximum efficiency.

2.3.2. Performance of turbine-generator set

The dynamics of the turbine-generator set were modelled following:

$$\frac{\mathrm{d}}{\mathrm{d}t}\left(\frac{1}{2}\, I\, \Omega^2\right) = P_t - P_g, \tag{10}$$

where I is the moment of inertia of the rotating parts; t is time; and P_g is the electromagnetic power of the generator imposed to control the rotational speed of the turbine. The moment of inertia of the turbine rotor can be scaled with its diameter according to Ref. [61]:

$$I = I_{ref}\left(\frac{D}{D_{ref}}\right)^5, \tag{11}$$

where I_{ref} and D_{ref} are the moment of inertia and diameter, respectively, with values corresponding to the biradial turbine installed at the Mutriku power plant within the OPERA H2020 project: $D_{ref} = 0.50$ m; $I_{ref} = 5.01$ kg m^2 [61].

2.3.3. Control system

The control law used in this work is based on the regulation of the rotational speed of the turbine [62], one of the simplest and most effective control strategies proposed for OWC devices, as reported in Ref. [61]. There are two operation modes: (i) regular and (ii) safe. During regular operation, the following control law is imposed at the generator:

$$P_g = a\, \Omega^b, \tag{12}$$

where a and b are the control parameters. A detailed sensitivity analysis of the effects of varying a and b on the pneumatic power, turbine power, electrical power and turbine efficiency for a biradial turbine is presented in Ref. [61]. This study concludes that the biradial turbine exhibits smooth behaviour and is able to operate close to its maximum performance over a broad range of control parameter values. On this basis, in the present analysis the control parameters were set to their values at the best efficiency point, namely $b = 3$; $a = a_{bep} = \rho_a \Pi_{bep} D^5$, where Π_{bep} is the power coefficient of the turbine at its point of maximum efficiency ($\Pi_{bep} = 0.027$). The variations in ρ_a are assumed to be negligible. To prevent exceeding the generator rated power, restrictions are introduced in Eq. (12) as follows:

$$P_g = \min\left(a_{bep}\, \Omega^3, P_{g,rated}\, , \Omega\, T_{g,max}\right), \tag{13}$$

where $P_{g,rated}$ is the rated power of the generator and $T_{g,max}$, the maximum allowed torque. The electrical generator considered in this work is a standard squirrel cage induction machine with rated power $P_{g,rated} = 30$ kW and a maximum allowed torque $T_{g,max} = 216.5$ N m [61]. The efficiency map of the generator (η_g) is presented in Fig. 5. The use of an efficiency map to evaluate the generator performance enables variations in the generator efficiency under different load conditions and rotational speeds to be explicitly accounted for, thereby providing a more accurate representation than the single efficiency curve commonly adopted in the modelling of OWC devices [63].

The system enters safe mode when the rotational speed exceeds an upper-threshold value:

$$\Omega_{max} = \min\left(\Omega_{g,max}, \Omega_{tip}\right), \tag{14}$$

where $\Omega_{g,max} = 314$ rad/s is the maximum rotational speed of the generator; and $\Omega_{tip} = 320/D$ rad/s is a term related to the maximum blade tip-speed, which is limited to 160 m/s. When this condition is reached, a safety valve installed in series with the turbine is closed. The control algorithm returns to regular operation, opening the safety valve, when the rotational speed is lower than a lower-threshold value:

$$\Omega_{thr} = \frac{\Omega_L}{2^{1/3}}, \tag{15}$$

where Ω_L is the rotational speed when the exponential part of the control law intersects the boundary of the operating region, defined by $P_{g,rated}/\Omega$ (Fig. 6).

2.3.4. Implementation

The turbine-generator set model uses the hydrodynamic results obtained from physical model testing as input data. Specifically, the experimentally measured pressure drop is employed, as it provides a reliable approximation of the turbine pressure drop. This is valid for self-rectifying impulse turbines—such as the biradial turbine—in which the rotational speed has a negligible effect on the turbine-induced damping.

The modelling process consists of several steps. First, the variables obtained experimentally are scaled to prototype dimensions. Second, the turbine diameter is determined using Eq. (9). Third, using the pressure drop time series, the turbine diameter and the performance curves of the biradial turbine (Fig. 4), Eq. (10) is applied to simulate the turbine-generator system in accordance with the selected control law (Eq. (13)). This step yields the rotational speed, power and control-imposed power of the turbine. Based on these outputs, the torque at the generator shaft is computed. Subsequently, by incorporating the performance characteristics of the generator (Fig. 5), the electrical efficiency is evaluated. Finally, the electrical power output and the total efficiency are calculated.

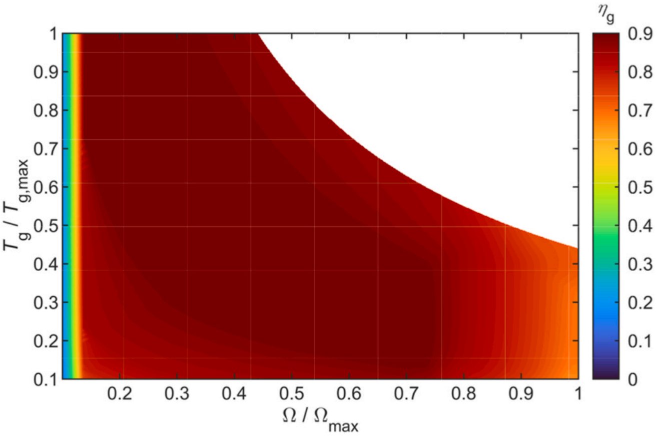

Fig. 5. Efficiency map of the electric generator (adapted from Ref. [64]).

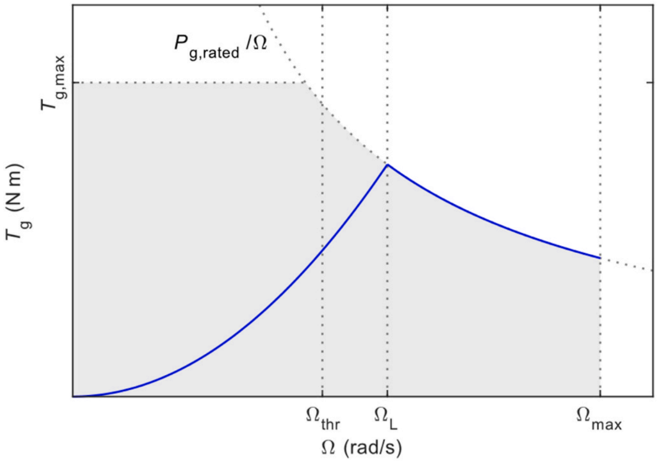

Fig. 6. Control law for the turbine-generator set operation. The shaded area represents the operating region, and the blue line an example control law.

2.4. Performance evaluation

The performance of the OWC device was evaluated, for each energy bin and for each damping condition, in terms of the time-averaged efficiency at each stage of the energy conversion process: pneumatic, mechanical and electrical efficiency. The time-averaged pneumatic efficiency, also referred to as the (hydrodynamic) capture-width ratio, is defined as the ratio of the pneumatic power extracted by the chamber to the incident wave power:

$$\overline{\eta}_{\mathrm{p}} = \frac{\overline{P}_{\mathrm{p}}}{w_{\mathrm{c}}\,\overline{P}_{\mathrm{w}}}, \tag{16}$$

where w_{c} is the width of the OWC chamber (in the direction parallel to the wave fronts); $\overline{P}_{\mathrm{p}}$ is the time-averaged pneumatic power, and $\overline{P}_{\mathrm{w}}$ is the average wave energy flux per metre of wave front. The time-averaged pneumatic power is computed as:

$$\overline{P}_{\mathrm{p}} = \frac{1}{t_{\mathrm{f}} - t_{\mathrm{i}}} \int_{t_{\mathrm{i}}}^{t_{\mathrm{f}}} \Delta p \, Q \, \mathrm{d}t, \tag{17}$$

where t_{i} and t_{f} denote the initial and final times of the time series, respectively.

The average wave energy flux is given by:

$$\overline{P}_{\mathrm{w}} = \rho_{\mathrm{w}}\, g \int_0^\infty S\, C_{\mathrm{g}}\, \mathrm{d}f, \tag{18}$$

where S is the incident spectral energy density and C_{g} is the group velocity of each frequency band.

The time-averaged mechanical efficiency is defined as the ratio of the time-averaged turbine power to the time-averaged pneumatic power:

$$\overline{\eta}_{\mathrm{m}} = \frac{\overline{P}_{\mathrm{t}}}{\overline{P}_{\mathrm{p}}}, \tag{19}$$

with the turbine power averaged over time as:

$$\overline{P}_{\mathrm{t}} = \frac{1}{t_{\mathrm{f}} - t_{\mathrm{i}}} \int_{t_{\mathrm{i}}}^{t_{\mathrm{f}}} P_{\mathrm{t}} \, \mathrm{d}t, \tag{20}$$

Similarly, the time-averaged electrical efficiency is defined as the ratio of the time-averaged electrical power output to the time-averaged turbine power:

$$\overline{\eta}_{\mathrm{e}} = \frac{\overline{P}_{\mathrm{e}}}{\overline{P}_{\mathrm{t}}}, \tag{21}$$

where the time-averaged electrical power is calculated as:

$$\overline{P}_{\mathrm{e}} = \frac{1}{t_{\mathrm{f}} - t_{\mathrm{i}}} \int_{t_{\mathrm{i}}}^{t_{\mathrm{f}}} \eta_{\mathrm{g}}\, P_{\mathrm{g}} \, \mathrm{d}t, \tag{22}$$

Additionally, stage-specific capture-width ratios are used to quantify the efficiency of the conversion from wave energy to each output stage. The hydrodynamic capture-width ratio is equal to the time-averaged pneumatic efficiency, and it is defined as $\xi_{\mathrm{h}} = \overline{\eta}_{\mathrm{p}}$. The aerodynamic capture-width ratio is given by:

$$\xi_{\mathrm{a}} = \frac{\overline{P}_{\mathrm{t}}}{w_{\mathrm{c}}\,\overline{P}_{\mathrm{w}}} = \overline{\eta}_{\mathrm{p}}\,\overline{\eta}_{\mathrm{m}}, \tag{23}$$

and the electrical capture-width ratio, representing the total (wave-to-wire) efficiency, is defined as:

$$\xi_{\mathrm{e}} = \frac{\overline{P}_{\mathrm{e}}}{w_{\mathrm{c}}\,\overline{P}_{\mathrm{w}}} = \overline{\eta}_{\mathrm{p}}\,\overline{\eta}_{\mathrm{m}}\,\overline{\eta}_{\mathrm{e}}\,. \tag{24}$$

In addition to the time-averaged parameters calculated for the individual sea states representative of each energy bin, annual-averaged performance parameters were also obtained. These were computed as a weighted sum of the time-averaged results for the sea states that define the wave climate at the case study site, with weights based on their occurrence. The annual-averaged parameters provide information on annual energy extraction and operational efficiency at each energy conversion stage. These annual-averaged parameters are denoted by using the subscript *annual*; for example, the annual-averaged hydrodynamic capture-width ratio is denoted as $\xi_{\mathrm{h,annual}}$.

3. Results and discussion

3.1. Numerical model validation

The numerical model was assessed by comparing measured and simulated time series of water column oscillations and pressure drop. Model performance was quantified by using the coefficient of determination (R^2) and the normalized root-mean-square error (NRMSE), as summarized in Table 1. The results demonstrate excellent agreement. Free-surface elevations show average NRMSE values below 0.05, while the pressure drop exhibits values around 0.06. In all cases, the mean R^2 exceeds 0.95, indicating a high level of correlation between the experimental and numerical datasets. Fig. 7 illustrates the correspondence for two selected cases, revealing that the model accurately captures both the oscillation amplitude and the phase relationship. Notably, good agreement is obtained even when the water column exhibits non-piston-like behaviour—i.e., when the front and rear free-surface elevations differ in amplitudes (red and black time series in Fig. 7). Similar performance is observed for all orifice diameters tested. Additional details regarding the numerical model validation are provided in Ref. [35].

Table 1
Mean and standard deviation of the coefficient of determination (R^2) and the normalized root-mean-square error (NRMSE) obtained in the numerical model validation tests for the pressure drop (Δp) and the free-surface elevations measured near the front and rear walls (z_1 and z_2, respectively).

		Mean	Standard deviation
$\boldsymbol{\Delta p}$	$\boldsymbol{R^2}$	0.957	0.012
	NRMSE	0.062	0.011
$\boldsymbol{z_1}$	$\boldsymbol{R^2}$	0.977	0.006
	NRMSE	0.047	0.007
$\boldsymbol{z_2}$	$\boldsymbol{R^2}$	0.975	0.007
	NRMSE	0.049	0.008

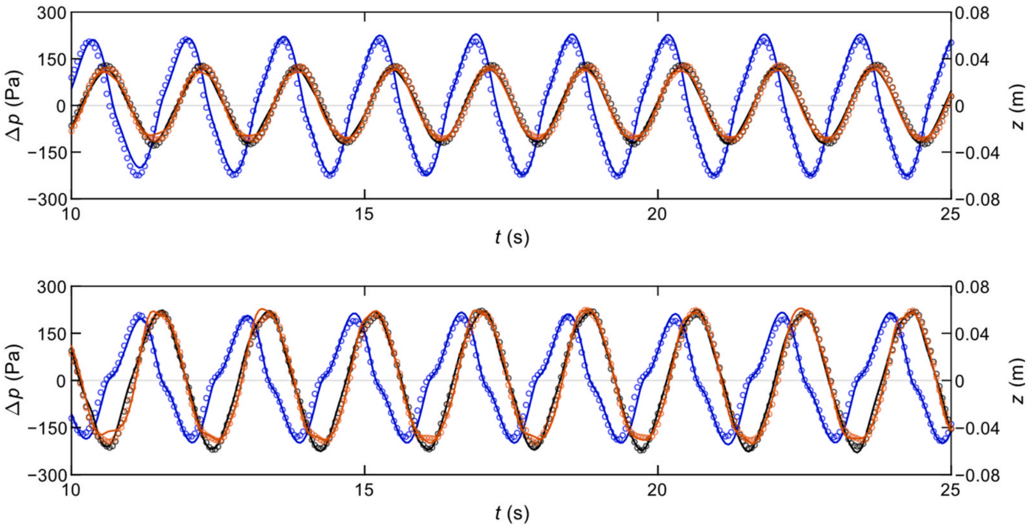

Fig. 7. Time series of pressure drop (Δp) (blue) and water column elevation (z) (black and red, measured near the front and rear walls, respectively) from experimental data (circles) and numerical model predictions (solid lines). Results are shown for (top panel) a wave condition with $H = 0.05$ m and $T = 1.64$ s, using an orifice diameter of $d = 17$ mm; and (bottom panel) a wave condition with $H = 0.067$ m and $T = 1.83$ s, using an orifice diameter of $d = 25$ mm.

3.2. Turbine-generator set modelling

The application of the methodology proposed to simulate the turbine-generator set is illustrated in Fig. 8 for a representative wave condition. Two turbines are analysed: one with a small diameter and lower rotor inertia, and the other with a large diameter and higher rotor inertia. A representative segment of the time series is shown to illustrate the turbine's behaviour during transitions into and out of safe mode.

Several key observations emerge from the results. First, the turbine diameter influences the damping introduced into the OWC system, which significantly alters the chamber behaviour and affects both the pressure drop and flow rate time-series. Specifically, increasing the turbine diameter (which reduces damping) results in lower pressure drop and higher airflow through the turbine. Consequently, the two configurations capture different amounts of pneumatic power. For the wave condition analysed, the larger turbine allows the chamber to capture on average more pneumatic power than its smaller counterpart ($\overline{P}_\mathrm{p} = 58.6$ kW vs. 53.3 kW, respectively).

Second, the smaller turbine responds more quickly to the variations in incident wave power, achieving significantly higher rotational speeds. On average, it operates at more than double the rotational speed of the larger turbine ($\Omega_\mathrm{average} = 186$ vs. 75 rad/s). As a result, the smaller turbine can occasionally exceed the upper threshold for safe operational speed, thereby triggering the safe mode mechanism—a situation that is adequately addressed by the implemented model. This behaviour arises from the lower rotor inertia of the smaller turbine. For turbines of similar geometry and constructed from comparable materials, rotor inertia scales approximately with the fifth power of the rotor diameter, D^5 [61]. Consequently, a reduction in turbine diameter leads to a substantial decrease in rotational inertia. Lower inertia corresponds to a shorter mechanical time constant [65], causing the turbine to respond more rapidly to short-term pressure fluctuations and thereby making overspeed events more likely.

Third, the operational differences between the turbines considerably impact the overall system performance. Despite capturing slightly more pneumatic power, the larger turbine yields less mechanical power on average due to its lower efficiency: $\overline{P}_\mathrm{t} = 17.3$ kW, vs. $\overline{P}_\mathrm{t} = 27.4$ kW for the smaller turbine. This outcome highlights the importance of considering the performance of the turbine when selecting the optimal damping level for a given OWC chamber design.

Finally, the influence of the generator is comparatively smaller, introducing only a minor reduction in the power output. For instance, in the case of the smaller turbine, the electrical power output is reduced to $\overline{P}_\mathrm{e} = 23.6$ kW; nevertheless, the overall performance trends observed at turbine level remain unchanged.

3.3. Influence of turbine-induced damping on the efficiency of the OWC device

To accurately represent the influence of the turbine-induced damping on the different energy conversion stages of an OWC device at a coastal site, it is necessary to consider the average efficiency across all sea states occurring over an average year (Fig. 9). The following analysis uses the site from Section 2.1, with wave characteristics shown in Fig. 1. Among the eight damping conditions tested, the turbine configuration that yields the highest annual pneumatic efficiency corresponds to a dimensionless damping coefficient $B_\mathrm{c} = 3.86$, associated with a turbine diameter of 1.3 m. For both lower and higher values of turbine-induced damping, pneumatic efficiency decreases—more sharply for lower damping values. The turbine-induced damping governs the balance between the amplitude of the water column oscillations and the resulting air pressure fluctuations within the chamber. When damping is too low, the chamber exhibits an underdamped behaviour: large air volume oscillations develop, but the associated pressure fluctuations are small, leading to reduced pneumatic efficiency (see Eqs. (16) and (17)) despite the significant internal motion. Conversely, when damping is excessively high, the airflow through the turbine is strongly restricted, suppressing the oscillatory motion of the water column and thereby limiting the capture of pneumatic power. The optimal damping condition therefore represents a compromise between maximizing water column excitation and chamber pressure response. An appropriate selection of the turbine diameter can result in improvements in annual-averaged pneumatic efficiency of up to 27 percentage points (e.g., $\overline{\eta}_\mathrm{p} = 0.56$ for $B_\mathrm{c} = 3.86$ vs $\overline{\eta}_\mathrm{p} = 0.29$ for $B_\mathrm{c} = 23.44$).

The mechanical efficiency does not follow the same trend as the pneumatic efficiency. For the range of damping conditions tested, higher damping values, or smaller turbine diameters, lead to higher mechanical efficiency. This behaviour, which has been reported in previous works [61], can be physically interpreted as a consequence of the reduced rotor inertia associated with smaller turbine diameters. As previously mentioned, rotor inertia scales strongly with diameter; consequently, smaller turbines are more responsive to the unsteady pneumatic power input imposed by irregular waves. The lower inertia allows the turbine rotational speed to track these variations more closely, enabling the

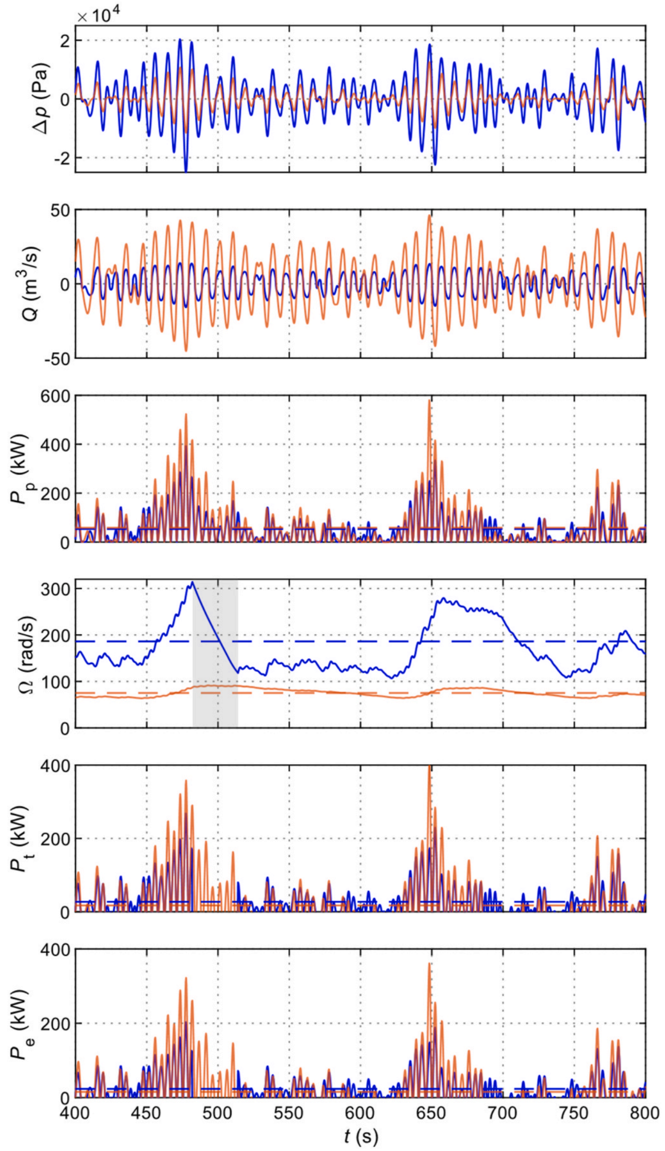

Fig. 8. Time series of pressure drop (Δp), flow rate (Q), and pneumatic power (P_p) obtained from physical modelling and scaled to prototype dimensions, together with turbine rotational speed (Ω), turbine power (P_t) and electrical power (P_e) derived from the turbine-generator set model, for a wave condition with significant wave height $H_{m0} = 2.6$ m and energy period $T_e = 8.5$ s. Results are presented for two turbine diameters: $D = 0.8$ m (blue line) and $D = 1.6$ m (red line). Dashed lines indicate time-average values. The shaded region in the turbine rotational speed plot denotes a zone in which the turbine entered in safe mode operation.

turbine to operate for longer periods near its best efficiency point, that is, at the instantaneous rotational speed that maximizes turbine efficiency. Although the control system continuously regulates the rotational speed towards its optimal value, in configurations with larger inertia (lower damping and larger diameter), the rotor responds more slowly to the variations in the aerodynamic conditions, leading to deviations from the optimal operating condition and increased losses. Accordingly, selecting an appropriate turbine diameter can result in gains of up to 25 percentage points in mechanical efficiency (e.g., $\overline{\eta}_m = 0.60$ for $B_c = 23.44$ vs. $\overline{\eta}_m = 0.35$ for $B_c = 1.89$).

The annual-averaged electrical efficiency exhibits a trend similar to that of the mechanical efficiency: higher values of the dimensionless damping coefficient correspond to higher electrical efficiency. Specifically, within the investigated operating range, the electrical efficiency increases with the dimensionless damping coefficient and then reaches a plateau at $B_c = 7.82$. Again, there are significant variations between the most and least efficient configurations ($\overline{\eta}_e = 0.88$ for $B_c = 7.82$ vs $\overline{\eta}_e = 0.57$ for $B_c = 1.89$). Nonetheless, the electrical efficiency curve displays a broader range of stable operation, maintaining values exceeding 80% for all damping coefficients above $B_c = 3.23$. In contrast, a significant drop in efficiency is observed for lower damping values. These lower damping values correspond to larger turbine diameters, which operate at significantly lower rotational speeds (see, for example, Fig. 8) and exhibit comparatively lower mechanical efficiency, thereby reducing the mechanical power delivered to the generator and resulting in lower generator loading. As a consequence, the generator operating point shifts towards a less efficient region (Fig. 5).

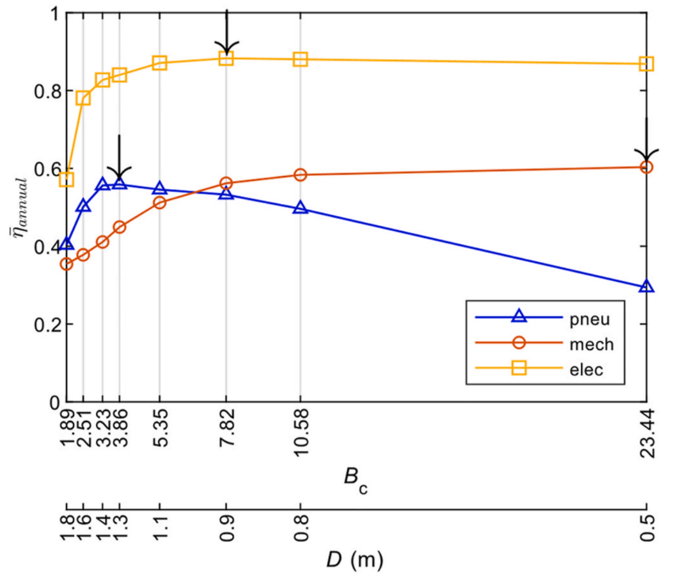

Fig. 9. Annual-averaged efficiencies of the OWC device as a function of the value of the dimensionless damping coefficient of the chamber (B_c) or the turbine diameter (D). The downward arrows indicate the maximum value of each efficiency.

The results presented in this work consider a single generator rated power. Although previous studies on biradial turbines indicate a limited sensitivity to the generator rated power [61], this aspect merits further investigation. In addition, the influence of the control law on electrical efficiency represents another relevant aspect, which has been also investigated in other studies (e.g., Refs. [64,66]) and is not examined in the present work.

After analysing the annual-averaged efficiencies, Fig. 10 presents the annual-averaged hydrodynamic, aerodynamic and electrical capture-width ratios for the pneumatic, mechanical and electrical stages, respectively. This performance metric enables the identification of the damping level that maximizes the performance of the OWC for each energy conversion stage. Although the hydrodynamic capture-with ratio is equivalent to the pneumatic efficiency discussed above, it is included to illustrate the trends across the capture-width ratio curves for each stage and to highlight the impact of the efficiency losses introduced at subsequent stages of energy conversion.

Two key findings merit discussion. First, turbine efficiency plays a critical role in determining the optimal turbine-chamber coupling. For the examined configuration of the turbine-generator set, turbine efficiency shifts the value of the dimensionless damping coefficient that maximizes the hydrodynamic capture-width ratio towards higher values, i.e., smaller turbine diameters. The maximum hydrodynamic capture-width ratio is $\xi_h = 0.56$, achieved for $B_c = 3.86$, whereas the maximum aerodynamic capture-width ratio is $\xi_a = 0.30$, achieved for $B_c = 7.82$. This result underscores the importance of incorporating the

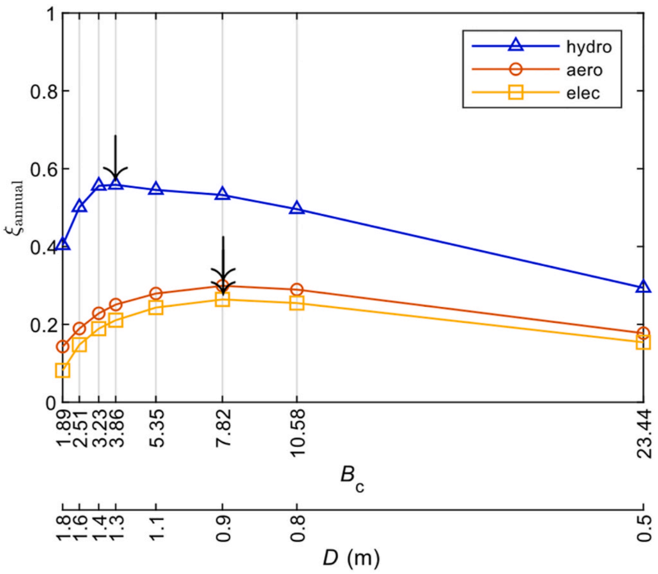

Fig. 10. Annual-averaged capture-width ratios of the OWC device as a function of the value of the dimensionless damping coefficient of the chamber (B_c) or the turbine diameter (D). The downward arrows indicate the maximum value of each capture-width ratio.

mechanical energy conversion stage into the turbine-chamber coupling process for OWC wave energy converters. Relying solely on the hydrodynamic capture-width ratio may be insufficient. Although this conclusion is based on a site-specific wave energy resource and should not be generalized (i.e., the damping that maximizes pneumatic efficiency may coincide under a particular wave climate with that which optimizes the mechanical performance), it strongly reinforces the need to account for turbine efficiency into the design assessment of OWC systems.

Second, the aerodynamic and electrical capture-width ratio curves follow the same trend. Although the generator efficiency slightly reduces the performance of the preceding energy conversion stage, it does not alter the damping value that yields maximum efficiency. Consequently, for the selection of the turbine-induced damping of an OWC at a particular coastal site, the influence of electrical efficiency on the optimal damping condition appears to be limited, as it is primarily governed by the mechanical stage. For the present case study, the maximum annual-averaged electrical capture-width ratio is $\xi_e = 0.26$, attained at $B_c = 7.82$, which corresponds to a turbine diameter of $D = 0.9$ m, consistent with the optimal aerodynamic capture-width ratio. The turbine diameter corresponding to this optimal damping is of the same order of magnitude as those reported in previous studies [61]. Notably, *ceteris paribus*, biradial turbines generally exhibit a smaller optimal diameter compared with Wells turbines [67].

Regarding the maximum annual-averaged electrical capture-width ratio, although it is slightly lower than the W2W efficiencies reported in related studies, typically in the range 0.35 to 0.40 (e.g., Refs. [61,67]), it should be noted that the present analysis considers a total of 27 sea states representing the full exploitable wave energy resource at the study site (see Fig. 1). In contrast, related works often focus only on the most energetic sea states, and thus most relevant for electricity production, generally represented by between 10 and 15 sea states (e.g., Refs. [61,67]). As a result, the annual-averaged performance indicators reported here, despite being more representative of long-term operation, yield lower values.

The results of this study have been obtained for a specific coastal site and its associated wave climate; consequently, the quantitative values reported—such as the optimal damping levels—are site-dependent and should not be generalized. The small-scale physical modelling involves inherent simplifications, including the emulation of turbine-induced damping by means of orifices, which may influence the pneumatic efficiency at full scale. In addition, the W2W approach adopts a static control strategy, and detailed structural, inertial and economic constraints are also not considered. Uncertainties associated with experimental measurements, numerical modelling and scaling effects are also present. Despite these limitations, this study provides valuable insight into the influence of turbine-induced damping on hydrodynamic, aerodynamic and electrical performance of OWCs, and provides a reference framework that can be extended to other sites. The influence of the variations in generator rated power and alternative control strategies constitute an important topic for future work.

3.4. *Performance matrices*

Finally, the performance of each energy conversion stage across the different wave conditions is analysed in Fig. 11. Three turbine-induced damping levels were selected: $B_c = 23.44$, 7.82 and 3.86, corresponding to turbine diameters $D = 0.5$, 0.9 and 1.3 m, respectively. This selection comprises the damping value that yields the maximum electrical capture-width ratio ($B_c = 7.82$), plus one higher and one lower value. In particular, the lower damping ($B_c = 3.86$) corresponds to the damping condition that maximizes the hydrodynamic capture-width ratio.

The first row of plots in Fig. 11 shows an improvement in the hydrodynamic capture-width ratio of the OWC for wave energy periods falling into the approximate range of 8 to 10 s. This behaviour is directly related to the chamber geometry, which was designed to operate in near-resonant conditions under these wave periods [51]. A comparison of the three plots highlights the influence of turbine-induced damping on the pneumatic efficiency of the chamber. The intermediate damping achieves the highest efficiency values, with values of the hydrodynamic capture-width ratio reaching $\xi_h = 0.82$, observed in the energy bin defined by $0 < H_{m0} < 1$ m and 8 s $< T_e < 9$ s. In general, for all three damping levels, the best performance is obtained at low significant wave heights ($H_{m0} < 3$ m). Although the intermediate damping coefficient achieves the highest values of the hydrodynamic capture-width ratio for individual energy bins, the lowest damping ($B_c = 3.86$) provides the best overall performance, as previously shown in Figs. 9 and 10. The better performance achieved for the higher wave heights ($H_{m0} > 2$ m) is the key aspect for the improved performance under this damping condition.

The situation changes when the mechanical efficiency is taken into account (second row of plots in Fig. 11). Overall, the trends observed in the hydrodynamic capture-width ratio matrices are preserved in the aerodynamic stage, but the performance figures are reduced due to turbine conversion losses. Importantly, the best overall performance shifts from the lowest damping to the intermediate one (see Fig. 10). For the three damping levels, the biradial turbine performs best at smaller wave heights ($H_{m0} < 3$ m). As a result, the intermediate damping condition, which already accumulates the best hydrodynamic performance across these smaller waves, emerges as the configuration delivering the highest overall mechanical energy capture. At the bin level, the intermediate damping yields better performance that the lowest damping in nearly all cases, except for the highest significant wave heights ($H_{m0} > 4$ m). The poorer results for the lowest damping can be attributed to the larger inertia associated with a bigger turbine diameter, which limits the ability of the turbine to adapt to rapid variations in wave forcing. Overall, the biradial turbine exhibits smooth performance across sea states. This behaviour, also reported for other self-rectifying impulse turbines, contrasts with the irregular energy capture patterns or pronounced performance peaks observed for Wells turbines under specific sea states [39,40], thereby highlighting the advantages of the biradial turbine.

Finally, in the electrical conversion stage (third row of plots in Fig. 11), the capture-width ratio is, in general, slightly reduced across all energy bins from that achieved at the aerodynamic stage, regardless of the damping condition considered. One notable exception is observed

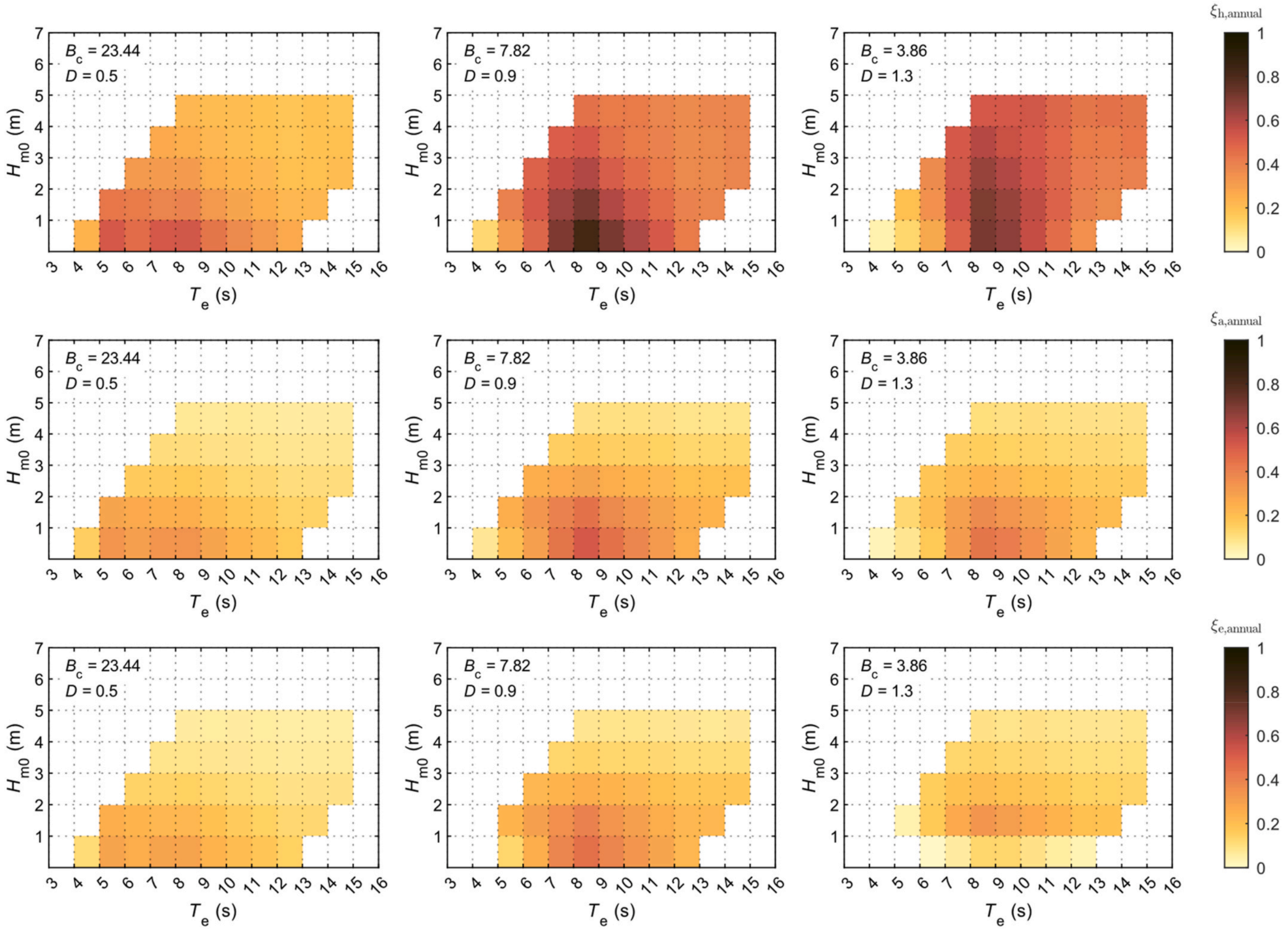

Fig. 11. Annual-averaged capture-width ratio matrices for three different turbine diameters (columns 1 to 3) considering the three energy conversion stages: hydrodynamic, aerodynamic and electrical (rows 1 to 3, respectively).

under the lowest damping condition, where the electrical capture-width ratio is strongly reduced for the smallest wave heights ($H_{m0} < 1$ m). Under these conditions, the turbine operates at excessively low rotational speeds, significantly reducing the generator performance (see Fig. 5).

4. Conclusions

In this study, the influence of turbine-induced damping on the successive energy conversion stages of an OWC device was assessed through a wave-to-wire model applied to a case study at a coastal site in Galicia (NW Spain). The methodology presented is applicable to non-linear impulse turbines, with a specific focus on the biradial turbine. The wave-to-wire model integrates multiple modelling approaches: (i) nearshore wave energy resources are characterized by means of high-resolution spectral numerical modelling; (ii) the hydrodynamic response of the device is evaluated through a combination of physical modelling and CFD modelling, explicitly accounting for air compressibility; and (iii) the turbine-generator set dynamics are represented analytically, imposing a control law based on the regulation of the rotational speed. This framework facilitates the evaluation of efficiency and capture-width ratio at each energy conversion stage: pneumatic, mechanical and electrical.

Based on the results of the case study, the following conclusions can be drawn. First, turbine-induced damping significantly influences OWC performance across all energy conversion stages. Second, the levels of damping that maximize mechanical efficiency or pneumatic efficiency are not the same. For the turbine-generator set considered, greater damping (corresponding to smaller turbine diameters) enhances the mechanical efficiency of the biradial turbine. Consequently, the optimum damping condition considering both mechanical and pneumatic efficiency shifts to values larger than those predicted by considering pneumatic performance alone. Specifically, for the coastal site of the present case study, the turbine-induced damping yielding maximum pneumatic energy capture is $B_c = 3.86$, corresponding to a turbine diameter of $D = 1.3$ m. In contrast, the maximum capture of mechanical and electrical energy occurs at $B_c = 7.82$, corresponding to a turbine diameter of $D = 0.9$ m. Third, although generator efficiency slightly diminishes the performance inherited from the mechanical stage, it does not alter the damping condition for the maximum efficiency within the investigated operating range.

When disaggregated by wave conditions, the best performance for the analysed site is achieved across all energy conversion stages for the wave periods close to the natural frequency of oscillation of the chamber ($8\text{ s} < T_e < 10\text{ s}$). With respect to wave height, performance is generally maximized for the smaller wave heights ($H_{m0} < 3$ m), with one exception: under low-damping configurations, the electrical capture-width ratio suffers a significant performance drop under the smaller wave heights due to insufficient turbine rotational speed.

Overall, the results obtained for this specific site and device configuration indicate that turbine efficiency plays a critical role in the optimal turbine-chamber coupling of OWC devices. This finding underscores the necessity of incorporating the mechanical energy conversion stage in the design process, rather than relying exclusively on the pneumatic efficiency. All in all, OWC chamber geometry should be designed not only to achieve near-resonant conditions under the most energetic site-specific wave conditions, but also to align the optimal damping condition with that which maximizes turbine efficiency, thereby enhancing the overall energy capture of the OWC system.

CRediT authorship contribution statement

I. López: Writing – original draft, Visualization, Software, Methodology, Investigation, Conceptualization. **B. Álvarez:** Writing – review & editing, Visualization, Validation, Investigation. **D.M. Fouz:** Writing – review & editing, Visualization, Validation, Software. **R. Carballo:** Writing – review & editing, Supervision, Methodology, Investigation, Funding acquisition. **G. Iglesias:** Writing – review & editing, Supervision.

Declaration of competing interest

The authors declare the following financial interests/personal relationships which may be considered as potential competing interests: Given his role as Editor of the journal, Prof. Gregorio Iglesias had no involvement in the peer review of this article and had no access to information regarding its peer review. Full responsibility for the editorial process for this article was delegated to another journal editor. If there are other authors, they declare that they have no known competing financial interests or personal relationships that could have appeared to influence the work reported in this paper.

Acknowledgements

This research was funded by the PORTOS project—Ports Towards Energy Self-Sufficiency—reference number EAPA_784/2018, co-financed by the Interreg Atlantic Area Program through the European Regional Development Fund and 'Axudas para a consolidación e estruturación de unidades de investigación competitivas nas universidades do Sistema Universitario de Galicia 2023' with reference number ED431B 2023/17. During this work D.M. Fouz was supported by the postdoctoral orientation period of a predoctoral grant of the 'Convocatoria de contratos predoutorais do Campus de Especialización Campus Terra' with reference number 8042 272B 64100 and 'Axudas para a consolidación e estruturación de unidades de investigación competitivas e outras accións de fomento nas universidades do Sistema Universitario de Galicia (2025-28)' with reference number ED431C 2025/17. The numerical model simulations have been performed on the FinisTerrae II supercomputer at the 'Centro de Supercomputación de Galicia (CESGA)'.

Data availability

Data will be made available on request.

References

[1] Gielen D, Boshell F, Saygin D, Bazilian MD, Wagner N, Gorini R. The role of renewable energy in the global energy transformation. Energy Strategy Rev 2019;24:38–50. https://doi.org/10.1016/j.esr.2019.01.006.

[2] Mørk G, Barstow S, Kabuth A, Pontes MT. Assessing the global wave energy potential. Shanghai, China: American Society of Mechanical Engineers Digital Collection; 2010. p. 447–54. https://doi.org/10.1115/OMAE2010-20473.

[3] Carballo R, Sánchez M, Ramos V, Taveira-Pinto F, Iglesias G. A high resolution geospatial database for wave energy exploitation. Energy 2014;68:572–83. https://doi.org/10.1016/j.energy.2014.02.093.

[4] Carballo R, Iglesias G. Wave farm impact based on realistic wave-WEC interaction. Energy 2013;51:216–29. https://doi.org/10.1016/j.energy.2012.12.040.

[5] Langhamer O, Haikonen K, Sundberg J. Wave power—Sustainable energy or environmentally costly? A review with special emphasis on linear wave energy converters. Renew Sustain Energy Rev 2010;14:1329–35. https://doi.org/10.1016/j.rser.2009.11.016.

[6] Iglesias G, Carballo R. Wave energy and nearshore hot spots: the case of the SE Bay of Biscay. Renew Energy 2010;35:2490–500. https://doi.org/10.1016/j.renene.2010.03.016.

[7] Arrosyid WA, Sari WR, Waskito KT, Yanuar Pria, Utama IKA, Binu Soesanto QM, et al. Recent advancements in wave energy converter technologies: a comprehensive review on design and performance optimization. Ocean Eng 2025;340:122328. https://doi.org/10.1016/j.oceaneng.2025.122328.

[8] Guo B, Ringwood JV. A review of wave energy technology from a research and commercial perspective. IET Renew Power Gener 2021;15:3065–90. https://doi.org/10.1049/rpg2.12302.

[9] Falcão AFO, Henriques JCC. Oscillating-water-column wave energy converters and air turbines: a review. Renew Energy 2016;85:1391–424. https://doi.org/10.1016/j.renene.2015.07.086.

[10] Zheng S, Zhang Y, Iglesias G. Coast/breakwater-integrated OWC: a theoretical model. Mar Struct 2019;66:121–35. https://doi.org/10.1016/j.marstruc.2019.04.001.

[11] Zhang X, Mayon R, Zhou F, Ning D. Experimental and numerical investigation on a novel dual-chamber OWC-WEC integrated with an energy-focusing breakwater. Coast Eng 2025;201:104814. https://doi.org/10.1016/j.coastaleng.2025.104814.

[12] Zhou Y, Ning D, Mayon R. Hydrodynamic loading analysis of an oscillating water column wave energy converter coupled with a land-fixed parabolic breakwater. Appl Ocean Res 2025;158:104594. https://doi.org/10.1016/j.apor.2025.104594.

[13] Konispoliatis DN. Hydrodynamic analysis of a dual chamber floating oscillating water column device. Appl Ocean Res 2025;154:104340. https://doi.org/10.1016/j.apor.2024.104340.

[14] Zheng S, Antonini A, Zhang Y, Miles J, Greaves D, Zhu G, et al. Hydrodynamic performance of a multi-oscillating water column (OWC) platform. Appl Ocean Res 2020;99. https://doi.org/10.1016/j.apor.2020.102168. 102168–102168.

[15] Zheng S, Michele S, Liang H, Iglesias G, Greaves D. Wave power extraction from a wave farm of tubular structure integrated oscillating water columns. Renew Energy 2024;225:120263. https://doi.org/10.1016/j.renene.2024.120263.

[16] Zheng S, Zhu G, Simmonds D, Greaves D, Iglesias G. Wave power extraction from a tubular structure integrated oscillating water column. Renew Energy 2020;150:342–55. https://doi.org/10.1016/j.renene.2020.01.008.

[17] Cui L, Zheng S, Zhang Y, Miles J, Iglesias G. Wave power extraction from a hybrid oscillating water column-oscillating buoy wave energy converter. Renew Sustain Energy Rev 2021;135. https://doi.org/10.1016/j.rser.2020.110234. 110234–110234.

[18] Michele S, Renzi E, Perez-Collazo C, Greaves D, Iglesias G. Power extraction in regular and random waves from an OWC in hybrid wind-wave energy systems. Ocean Eng 2019;191:106519. https://doi.org/10.1016/j.oceaneng.2019.106519.

[19] Perez-Collazo C, Greaves D, Iglesias G. A novel hybrid wind-wave energy converter for jacket-frame substructures. Energies 2018;11. https://doi.org/10.3390/en11030637.

[20] Jayashankar V, Anand S, Geetha T, Santhakumar S, Kumar VJ, Ravindran M, et al. A twin unidirectional impulse turbine topology for OWC based wave energy plants. Renew Energy 2009;34:692–8. https://doi.org/10.1016/j.renene.2008.05.028.

[21] Rodríguez L, Pereiras B, García-Diaz M, Fernández-Oro J, Castro F. Flow pattern analysis of an outflow radial turbine for twin-turbines-OWC wave energy converters. Energy 2020;211:118584. https://doi.org/10.1016/j.energy.2020.118584.

[22] Ansarifard N, Fleming A, Henderson A, Kianejad SS, Chai S, Orphin J. Comparison of inflow and outflow radial air turbines in vented and bidirectional OWC wave energy converters. Energy 2019;182:159–76. https://doi.org/10.1016/j.energy.2019.06.041.

[23] Joensen B, Bingham HB, Read RW, Nielsen K, Trevino JB. Hydrodynamic analysis of one-way energy capture by an oscillating water column wave energy device. Energy Rep 2023;9:5306–22. https://doi.org/10.1016/j.egyr.2023.04.052.

[24] Falcão AFO, Henriques JCC, Gato LMC. Self-rectifying air turbines for wave energy conversion: a comparative analysis. Renew Sustain Energy Rev 2018;91:1231–41. https://doi.org/10.1016/j.rser.2018.04.019.

[25] Shehata AS, Xiao Q, Saqr KM, Alexander D. Wells turbine for wave energy conversion: a review. Int J Energy Res 2017;41:6–38. https://doi.org/10.1002/er.3583.

[26] Setoguchi T, Santhakumar S, Maeda H, Takao M, Kaneko K. A review of impulse turbines for wave energy conversion. Renew Energy 2001;23:261–92. https://doi.org/10.1016/S0960-1481(00)00175-0.

[27] Carrelhas AAD, Gato LMC, Henriques JCC, Falcão AFO, Varandas J. Test results of a 30 kW self-rectifying biradial air turbine-generator prototype. Renew Sustain Energy Rev 2019;109:187–98. https://doi.org/10.1016/j.rser.2019.04.008.

[28] Falcão AFO, Gato LMC, Nunes EPAS. A novel radial self-rectifying air turbine for use in wave energy converters. Renew Energy 2013;50:289–98. https://doi.org/10.1016/j.renene.2012.06.050.

[29] López I, Pereiras B, Castro F, Iglesias G. Holistic performance analysis and turbine-induced damping for an OWC wave energy converter. Renew Energy 2016;85:1155–63. https://doi.org/10.1016/j.renene.2015.07.075.

[30] López I, Pereiras B, Castro F, Iglesias G. Performance of OWC wave energy converters: influence of turbine damping and tidal variability. Int J Energy Res 2015;39:472–83. https://doi.org/10.1002/er.3239.

[31] López I, Castro A, Iglesias G. Hydrodynamic performance of an oscillating water column wave energy converter by means of particle imaging velocimetry. Energy 2015;83:89–103. https://doi.org/10.1016/j.energy.2015.01.119.

[32] López I, Iglesias G. Efficiency of OWC wave energy converters: a virtual laboratory. Appl Ocean Res 2014;44:63–70. https://doi.org/10.1016/j.apor.2013.11.001.

[33] López I, Pereiras B, Castro F, Iglesias G. Optimisation of turbine-induced damping for an OWC wave energy converter using a RANS-VOF numerical model. Appl Energy 2014;127:105–14. https://doi.org/10.1016/j.apenergy.2014.04.020.

[34] López I, Carballo R, Iglesias G. Site-specific wave energy conversion performance of an oscillating water column device. Energy Convers Manag 2019;195:457–65. https://doi.org/10.1016/j.enconman.2019.05.030.

[35] López I, Carballo R, Fouz DM, Iglesias G. Non-linear turbine selection for an OWC wave energy converter. Ocean Eng 2024;311:118877. https://doi.org/10.1016/j.oceaneng.2024.118877.

[36] Gubesch E, Abdussamie N, Penesis I, Chin C. Maximising the hydrodynamic performance of offshore oscillating water column wave energy converters. Appl Energy 2022;308:118304. https://doi.org/10.1016/j.apenergy.2021.118304.

[37] Rezanejad K, Anastas G, Hashemzadeh M, Gadelho JFM, López I, Carballo R, et al. Experimental study on the hydrodynamic performance of an innovative floating dual-chamber oscillating water column. Ocean Eng 2025;323:120549. https://doi.org/10.1016/j.oceaneng.2025.120549.

[38] Penalba M, Ringwood JV, Penalba M, Ringwood JV. A review of wave-to-wire models for wave energy converters. Energies 2016;9. https://doi.org/10.3390/en9070506.

[39] Ciappi L, Simonetti I, Bianchini A, Cappietti L, Manfrida G. Application of integrated wave-to-wire modelling for the preliminary design of oscillating water column systems for installations in moderate wave climates. Renew Energy 2022; 194:232–48. https://doi.org/10.1016/j.renene.2022.05.015.

[40] Ciappi L, Cheli L, Simonetti I, Bianchini A, Talluri L, Cappietti L, et al. Wave-to-wire models of wells and impulse turbines for oscillating water column wave energy converters operating in the Mediterranean Sea. Energy 2022;238:121585. https://doi.org/10.1016/j.energy.2021.121585.

[41] Rosati M, Ringwood JV. Wave-to-Wire efficiency maximisation for oscillating-water-column systems. IFAC-PapersOnLine 2023;56:10886–91. https://doi.org/10.1016/j.ifacol.2023.10.769.

[42] Liu Z, Xu C, Kim K, Choi J, Hyun B. An integrated numerical model for the chamber-turbine system of an oscillating water column wave energy converter. Renew Sustain Energy Rev 2021;149:111350. https://doi.org/10.1016/j.rser.2021.111350.

[43] Liu Z, Xu C, Kim K. A CFD-based wave-to-wire model for the oscillating water column wave energy convertor. Ocean Eng 2022;248:110842. https://doi.org/10.1016/j.oceaneng.2022.110842.

[44] Ding Z, Ning D, Mayon R. Wave-to-wire model for an oscillating water column wave energy converter. Appl Energy 2025;377:124663. https://doi.org/10.1016/j.apenergy.2024.124663.

[45] Ning D, Ding Z, Mayon R, Ruan H, Fu Y. Experimental and numerical investigation of resistive load impact on oscillating water column wave energy converter integrated with a parabolic breakwater. Energy 2025;324:135960. https://doi.org/10.1016/j.energy.2025.135960.

[46] Carballo R, López I, Areán N, Fouz DM. Technology-site selection based on high-resolution performance analysis. Universidade de Santiago de Compostela; 2020.

[47] Carballo R, Arean N, Álvarez M, López I, Castro A, López M, et al. Wave farm planning through high-resolution resource and performance characterization. Renew Energy 2019;135:1097–107. https://doi.org/10.1016/j.renene.2018.12.081.

[48] Silva D, Rusu E, Soares CG. Evaluation of various technologies for wave energy conversion in the Portuguese nearshore. Energies 2013;6:1344–64. https://doi.org/10.3390/en6031344.

[49] López I, Carballo R, Taveira-Pinto F, Iglesias G. Sensitivity of OWC performance to air compressibility. Renew Energy 2020;145:1334–47. https://doi.org/10.1016/j.renene.2019.06.076.

[50] Rezanejad K, Souto-Iglesias A, Guedes Soares C. Experimental investigation on the hydrodynamic performance of an L-shaped duct oscillating water column wave energy converter. Ocean Eng 2019;173:388–98. https://doi.org/10.1016/j.oceaneng.2019.01.009.

[51] López I, Carballo R, Fouz DM, Iglesias G. Design selection and geometry in OWC wave energy converters for performance. Energies 2021;14. https://doi.org/10.3390/en14061707. 1707–1707.

[52] Hughes SA. Physical models and laboratory techniques in coastal engineering, vol. 7. Singapore: World Scientific; 1993.

[53] Molina–Salas A, Longo S, Clavero M, Moñino A. Theoretical approach to the scale effects of an OWC device. Renew Energy 2023;219:119579. https://doi.org/10.1016/j.renene.2023.119579.

[54] Falcão AFO, Henriques JCC. The spring-like air compressibility effect in oscillating-water-column wave energy converters: review and analyses. Renew Sustain Energy Rev 2019;112:483–98. https://doi.org/10.1016/j.rser.2019.04.040.

[55] Falcão AFO, Henriques JCC. Model-prototype similarity of oscillating-water-column wave energy converters. Int J Mar Energy 2014;6:18–34. https://doi.org/10.1016/j.ijome.2014.05.002.

[56] Jasak H, Jemcov A, Tukovic Z. OpenFOAM: a C++ library for complex physics simulations. 2007. p. 1–20. Dubrovnik.

[57] Jacobsen NG, Fuhrman DR, Fredsøe J. A wave generation toolbox for the open-source CFD library: openfoam®. Int J Numer Methods Fluid 2012;70:1073–88. https://doi.org/10.1002/fld.2726.

[58] Menter FR, Kuntz M, Langtry R. Ten years of industrial experience with the SST turbulence model. Turbul Heat Mass Transf 2003;4:625–32.

[59] Pereiras B, López I, Castro F, Iglesias G. Non-dimensional analysis for matching an impulse turbine to an OWC (oscillating water column) with an optimum energy transfer. Energy 2015;87:481–9. https://doi.org/10.1016/j.energy.2015.05.018.

[60] Gato LMC, Henriques JCC, Carrelhas AAD, Lopes BS, Varandas J, Fay FX. Turbine and electrical equipment performance and reliability in shoreline OWC wave plant. Lisbon: Instituto Superior Técnico; 2018.

[61] Henriques JCC, Portillo JCC, Sheng W, Gato LMC, Falcão AFO. Dynamics and control of air turbines in oscillating-water-column wave energy converters: analyses and case study. Renew Sustain Energy Rev 2019;112:571–89. https://doi.org/10.1016/j.rser.2019.05.010.

[62] Falcão AF de O. Control of an oscillating-water-column wave power plant for maximum energy production. Appl Ocean Res 2002;24:73–82. https://doi.org/10.1016/S0141-1187(02)00021-4.

[63] Carrelhas AAD, Gato LMC, Henriques JCC, Marques GD. Estimation of generator electrical power output and turbine torque in modelling and field testing of OWC wave energy converters. Energy Convers Manag X 2023;19:100384. https://doi.org/10.1016/j.ecmx.2023.100384.

[64] Carrelhas AAD, Gato LMC. Reliable control of turbine–generator set for oscillating-water-column wave energy converters: numerical modelling and field data comparison. Energy Convers Manag 2023;282:116811. https://doi.org/10.1016/j.enconman.2023.116811.

[65] Rosati M, Ringwood JV, Henriques JCC. A comprehensive wave-to-wire control formulation for oscillating water column wave energy converters. Trends renew. Energ. Offshore. CRC Press; 2022.

[66] Faÿ F-X, Henriques JC, Kelly J, Mueller M, Abusara M, Sheng W, et al. Comparative assessment of control strategies for the biradial turbine in the Mutriku OWC plant. Renew Energy 2020;146:2766–84. https://doi.org/10.1016/j.renene.2019.08.074.

[67] Scialò A, Henriques JCC, Malara G, Falcão AFO, Gato LMC, Arena F. Power take-off selection for a fixed U-OWC wave power plant in the Mediterranean Sea: the case of Roccella Jonica. Energy 2021;215. https://doi.org/10.1016/j.energy.2020.119085. 119085–119085.